Observation of Chiral Surface Excitons in a Topological Insulator Bi_2Se_3

H.-H. Kung[a,1,2], **A. P. Goyal**[b], **D. L. Maslov**[b,1], **X. Wang**[a,c], **A. Lee**[a], **A. F. Kemper**[d], **S.-W. Cheong**[a,c], **and G. Blumberg**[a,e,1]

[a]Department of Physics & Astronomy, Rutgers University, Piscataway, NJ 08854, USA; [b]Department of Physics, University of Florida, Gainesville, FL 32611, USA; [c]Rutgers Center for Emergent Materials, Rutgers University, Piscataway, NJ 08854, USA; [d]Department of Physics, North Carolina State University, Raleigh, NC 27695, USA; [e]National Institute of Chemical Physics and Biophysics, Akadeemia tee 23, 12618 Tallinn, Estonia

This manuscript was compiled on May 8, 2019

The protected electron states at the boundaries or on the surfaces of topological insulators (TIs) have been the subject of intense theoretical and experimental investigations. Such states are enforced by very strong spin-orbit interaction in solids composed of heavy elements. Here, we study the composite particles – *chiral excitons* – formed by the Coulomb attraction between electrons and holes residing on the surface of an archetypical three-dimensional topological insulator (TI), Bi_2Se_3. Photoluminescence (PL) emission arising due to recombination of excitons in conventional semiconductors is usually unpolarized because of scattering by phonons and other degrees of freedom during exciton thermalization. On the contrary, we observe almost perfectly polarization-preserving PL emission from chiral excitons. We demonstrate that the chiral excitons can be optically oriented with circularly polarized light in a broad range of excitation energies, even when the latter deviate from the (apparent) optical band gap by hundreds of meVs, and that the orientation remains preserved even at room temperature. Based on the dependences of the PL spectra on the energy and polarization of incident photons, we propose that chiral excitons are made from massive holes and massless (Dirac) electrons, both with chiral spin textures enforced by strong spin-orbit coupling. A theoretical model based on such proposal describes quantitatively the experimental observations. The optical orientation of novel composite particles, the chiral excitons, can potentially expand applications of TIs in photonics and optoelectronics.

exciton | topological insulator | photoluminescence spectroscopy

Spin orbit coupling (SOC) plays a central role in spintronic and optoelectronic applications by allowing optical control of spin excitation and detection with circularly polarized light, in the absence of an external magnetic field (1–3). This effect is also known as optical orientation, where non-equilibrium distribution of spin-polarized quasiparticles are optically created in semiconductors with strong SOC (4, 5). Detailed information on spin dynamics can be obtained by studying polarized photoluminescence (PL) (6–9). Typically, the degree of PL polarization in semiconductors decreases rapidly as the excitation photon energy deviates from the optical band gap or with heating (4, 5, 10). Elaborative layer and strain engineering are often required to lift spin degeneracy of the bulk bands to achieve higher degree of PL polarization (11). In contrast, nearly complete PL polarization, observed recently in transition metal dichalcogenide (TMD) monolayers up to room temperature, was attributed to spin-orbit mediated coupling between the spin and valley degrees of freedom (12–14). The reduced dimensionality suppresses dielectric screening and restricts the number of scattering channels, resulting in long-lived coherent two-dimensional (2D) excitons (15). These results have attracted significant interest due to possible applications and also as an insight into the nature of many body interactions in 2D electronic and photonic systems (3, 13, 16).

In this paper, we discuss a new class of excitons which produce helicity preserving PL. We use polarization-resolved PL spectroscopy to study the secondary emission from a 2D electronic system of significant current interest: the surface state of a three-dimensional (3D) topological insulator (TI), Bi_2Se_3.* In 3D TIs, strong SOC and time-reversal symmetry collaborate to support topologically protected massless surface states [denoted by SS1 in Figs. 1(a) and (b)] with chiral spin-momentum texture (19–23). Both angular-resolved photoemission (ARPES) data and first-principle calculations show that there are two more surface bands near the Brillouin zone center (Γ-point) in Bi_2Se_3 (17, 18, 24): (1) a high-energy unoccupied Dirac cone (SS2) and (2) fully occupied Rashba-like surface states (RSS). These bands are depicted by red lines in Fig. 1(a) and enclosed in boxes in Fig. 1 (b). Due to strong SOC, all the three surface bands exhibit spin-momentum locking, which could lead to optical orientation of single-electron spins and excitons (4). So far, most of research on TIs have been focused on spin dynamics and collective modes of Dirac fermions in SS1 (25–28), and far less is known about the properties of RSS and SS2. We excite interband transitions between

*Polarized PL was also observed in $Bi_{1.95}In_{0.05}Se_3$ crystals [See *SI Appendix*, Sec. S3].

Significance Statement

We observe novel composite particles – *chiral excitons* – residing on the surface of a topological insulator (TI), Bi_2Se_3. Unlike other known excitons composed of massive quasiparticles, chiral excitons are the bound states of surface massless electrons and surface massive holes, both subject to strong spin-orbit coupling which locks their spins and momenta into chiral textures. Due to this unusual feature, chiral excitons emit circularly polarized secondary light (photoluminescence) that conserves the polarization of incident light. This means that the out-of-plane angular momentum of a chiral exciton is preserved against scattering events during thermalization, thus enabling optical orientation of carriers even at room temperature. The discovery of chiral excitons adds to the potential of TIs as a platform for photonics and optoelectronics devices.

G.B. designed and supervised the experiments. H.-H.K, A.L. and G.B. acquired and analyzed the data. A.G. and D.L.M. developed the theoretical model of chiral excitons. X.W. and S.-W.C. grew the single crystals. A.F.K. performed first-principle calculations of the band structure. All authors contributed to the discussion and writing of the manuscript.

The authors declare no conflict of interest.

[1]To whom correspondence should be addressed. E-mail: skung@physics.rutgers.edu, maslov@phys.ufl.edu and girsh@physics.rutgers.edu

[2]Present address: Quantum Matter Institute, University of British Columbia, Vancouver, BC, Canada.

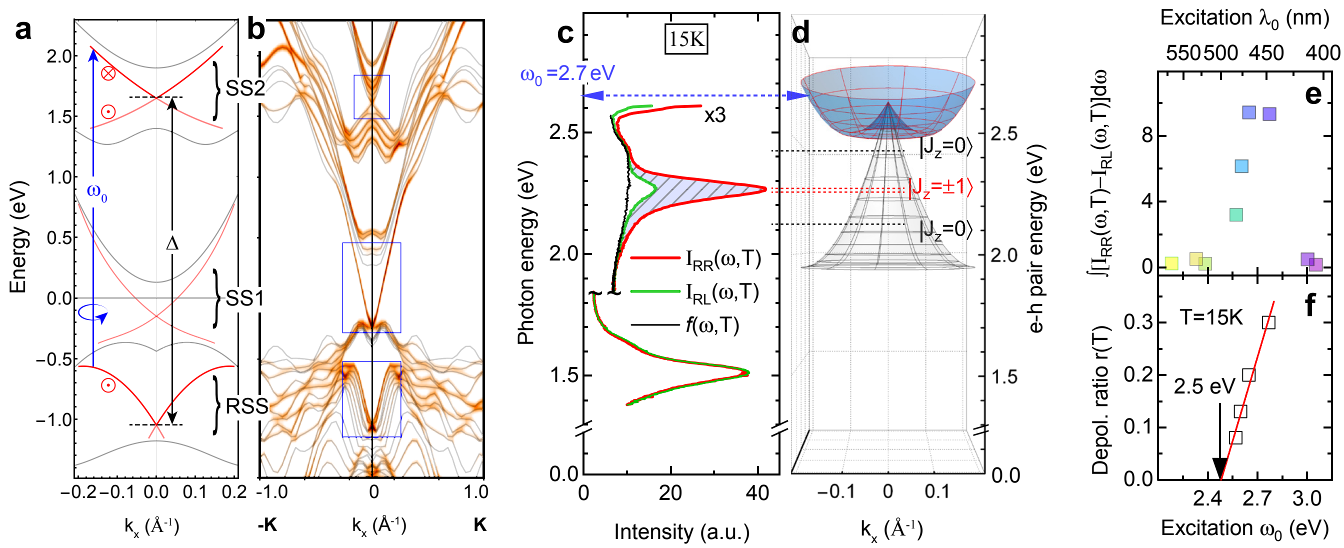

Fig. 1. (a) The electronic band structure near the Γ point as inferred from ARPES measurements (17, 18). The Rashba surface states (RSS) and the unoccupied topological surface states (SS2) are depicted by thick red lines, with the in-plane spin orientations denoted by $\odot$ and $\otimes$. The low energy surface states (SS1) near the Fermi energy (E_F) are depicted by thin red lines. The bulk bands (which do not contribute to circularly polarized PL) and are shown in gray. (b) Calculated band structure along the Γ–K cut in the Brillouin zone of the hexagonal lattice, projected onto the top QL for $J_z = 1/2$. The blue squares highlight the 3 surface bands [See *SI Appendix* Sec. S2]. (c) The PL spectra measured with right-circularly polarized 2.7 eV excitation at 15 K. Right- and left-circularly polarized PL signals are designated by $I_{\rm RR}(\omega, T)$ in red, and $I_{\rm RL}(\omega, T)$ in green, respectively. The black line shows unpolarized PL background, $f(\omega, T)$. The intensity in the 1.8–2.6 eV range is multiplied by factor of 3 for clarity. (d) The dispersion relation of non-interacting electron-hole pairs for possible transitions from RSS to SS2, with zero momentum transfer. The only transition consistent with the excitation energy employed in this study is shown in blue, otherwise shown in gray. With finite interaction, the excitonic bound states form below the band minimum, and are denoted by the total angular momenta of the electron-hole pairs, J_z. (e) The integrated polarized PL intensity, $\int_{2.0}^{2.5\,eV}[I_{\rm RR}(\omega, T) - I_{\rm RL}(\omega, T)]d\omega$ [shown as the shaded blue area in (c)], versus excitation energy measured at 15 K. (f) The depolarization ratio $r(T) \equiv \frac{I_{\rm RL}(\omega,T)-f(\omega,T)}{I_{\rm RR}(\omega,T)-f(\omega,T)}$ is plotted as a function of (ω_0), with $T \approx 15\,$K. The red line is a linear extrapolation to $r(T) = 0$, suggesting a minimum excitation threshold energy of 2.5 eV.

surface states, RSS and SS2, with circularly polarized light, and study polarization of PL emission in the backscattering geometry, with light being incident normally on the crystal surface.

Experimental results

Polarized photoluminescence. Figure 1(c) depicts the intensities of right- and left-circularly polarized PL signals excited by right-circularly polarized light, $I_{\rm RR}(\omega, T)$ and $I_{\rm RL}(\omega, T)$, respectively, where ω is the energy of emitted photons and T is temperature. Two emission peaks at about 1.5 and 2.3 eV in the visible range behave in a strikingly different ways when excited by circularly polarized light. Namely, the peak at 1.5 eV is unpolarized, i.e., emission of right- and left-circularly polarized light has same intensity. The peak at 1.5 eV behaves as an ordinary PL signal observed in conventional semiconductors, where the memory about the incident photon polarization is lost during thermalization of optically generated electron-hole pairs. In contrast, the peak at 2.3 eV is almost fully polarized with the same polarization as the excitation photon, i.e., emission occurs in the *RR* channel but not in the *RL* one.

We note that excitons are not usually observed in semimetals and doped semiconductors, with the Fermi level crossing the conduction band, because the exciton state is likely to be hybridized with the conduction band states. Even if the exciton level remains within the gap, the optically produced electron-hole pairs would relax rapidly to the Fermi energy in a non-radiative way. In our case, RSS and SS2 are gapped from the Fermi level, and thus the electron-hole bound state can decay radiatively, resulting in observed PL.

To further elucidate the nature of polarized PL in Bi_2Se_3, we compare the spectra measured in different polarization geometries. The results are reproducible in the "time-reversed" geometry, i.e., the polarized PL signals with right- [Fig. 2(a)] and left-circularly polarized excitation [Fig. 2(b)] show the same line shape and intensity. This suggests that the light-emitting states are doubly degenerate, with components amenable to independent excitation by right- or left circularly-polarized photons. If relaxation processes of these states preserve their angular momenta, the secondary photons are emitted with the same polarization as the excitation one. For reasons that will become clear later on, we denote these states as $|J_z = 1\rangle$ and $|J_z = -1\rangle$ [Fig. 1(d)].

In Fig. 2(c)–(f) we show intensity of PL excited with linearly polarized light, with X (Y) denoting linear polarization parallel (orthogonal) to the plane of incidence. We find that the PL signal has almost the same intensity and line shape in both circular polarization channels, regardless of whether the excitation photon is X or Y polarized [Fig. 2(c)–(e)]. This suggests that a linearly polarized photon, being decomposed into right- and left-circularly polarized ones, can independently excite both the $|J_z = 1\rangle$ and $|J_z = -1\rangle$ states. That linear polarization is not preserved in the PL process [Fig. 2(f)], and that $I_{\rm XL}(\omega, T)$ coincides with $[I_{\rm RL}(\omega, T) + I_{\rm LL}(\omega, T)]/2$ [Fig. 2(c)], imply that quantum coherence is not preserved during the relaxation of electron-hole pairs. As the result, the $|J_z = 1\rangle$ and $|J_z = -1\rangle$ excitonic states act as two independent emitters, which preserve linear but not circular polarization. This property of emission from Bi_2Se_3 surface states is in contrast to polarized PL observed in TMD monolayers, where

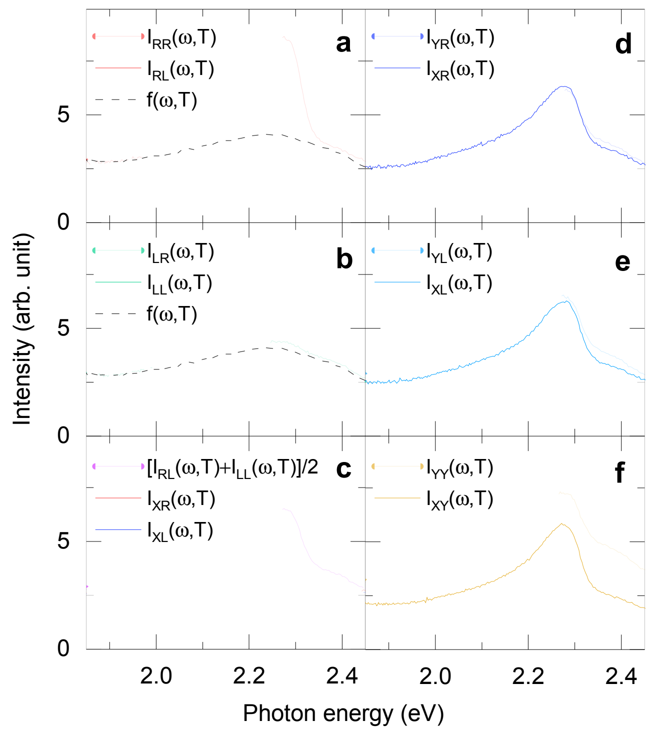

Fig. 2. Polarization dependence of PL measured with 2.6 eV excitation at 26 K. (a)–(b), The thick and thin lines show the right- and left-handed PL spectra under right- and left-circularly polarized excitation. The black line shows the unpolarized background. Panels (c)–(e) compare circularly polarized PL spectra excited with linearly polarized light, where X (Y) denotes linear polarization parallel (orthogonal) to the plane of incidence. (f), Comparison of the spectra with excitation polarization parallel and orthogonal to the PL polarization.

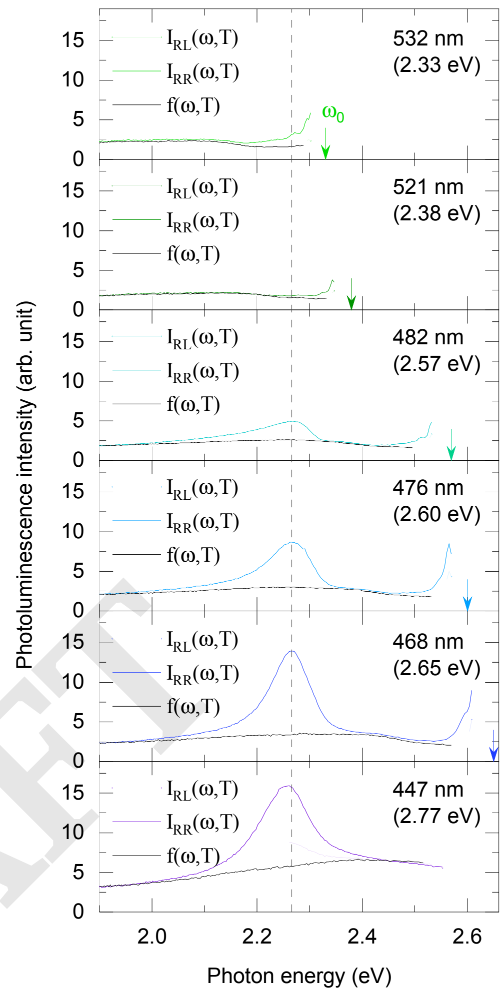

Fig. 3. Low temperature PL intensity is plotted against photon energy for 6 different excitations (shown by arrows in each panel): ω_0 =2.33, 2.38, 2.57, 2.60, 2.65 and 2.77 eV. The light and dark colored lines denotes $I_{\mathrm{RL}}(\omega, T)$ and $I_{\mathrm{RR}}(\omega, T)$, respectively. The smooth background $f(\omega, T)$ is plotted by black lines.

both circular and linear polarization are preserved due to valley quantum coherence (13, 14).

Dependence on the energy of incident photons. Such a high degree of circular polarization for PL cannot originate from the bulk bands, which are spin degenerate (29). However, all the three surface bands in Fig. 1(a) and (b) exhibit spin-momentum locking, and could lead to optical orientation of spins with circularly polarized light. To identify the electron bands responsible for polarized PL, we study the excitation dependence of the peak intensity. Figure 3 depicts the intensity of polarized PL measured with a right-circular excitation with six different energies, as denoted by the arrows in each panel. As one can see from the figure, the polarized PL peak, whose position is marked by the dashed line, is absent for excitation energies below 2.4 eV. This implies that the electron and hole bands involved in forming the exciton are separated by at least 2.4 eV. By comparing the PL spectra in the top two panels of Fig. 3, we note however that the spectrum for the excitation energy of 2.38 eV does not exhibit any visible features at the exciton energy, i.e. at 2.3 eV, whereas weak PL for the excitation energy of 2.33 eV is enhanced at 2.3 eV. Also, the enhancement occurs primarily in the polarized (RR) channel, whereas PL at the excitation energy of 2.38 eV is not polarized. We argue that this re-entrant behavior is an indication of the resonant excitation of dipole-allowed exciton states (30).

Besides the overall intensity, the difference between $I_{\mathrm{RL}}(\omega, T)$ and $I_{\mathrm{RR}}(\omega, T)$, depicted in Fig. 3 by the light and dark colored lines, respectively, also changes with the excitation energy. In Fig. 1(e) we show the integrated PL intensity difference, $\int_{2.0}^{2.5\,eV}[I_{\mathrm{RR}}(\omega,T) - I_{\mathrm{RL}}(\omega,T)]d\omega$, versus the excitation energy ω_0. The polarized PL peak is observed only for excitation energies between 2.6 and 3.0 eV. Comparing the excitation profile with the known band structure of Bi_2Se_3 [See *SI Appendix*, Sec. S2], we conclude that the only possible interband transition is from RSS to SS2 bands.

Depolarization. To analyze polarization-preserving PL quantitatively, we decompose $I_{\mathrm{RR}}(\omega, T)$ and $I_{\mathrm{RL}}(\omega, T)$ into two spectral contributions [Fig. 3]: (1) a broad unpolarized emission band, $f(\omega, T)$, and (2) a narrower peak that is almost fully polarized, with intensity defined as $\mathcal{L}_R(\omega, T) = I_{\mathrm{RR}}(\omega, T) - f(\omega, T)$. We note that $f(\omega, T)$ and $\mathcal{L}_R(\omega, T)$ have distinct lineshapes and therefore are likely to have different origins. We will henceforth focus on the polarized PL signal, $\mathcal{L}_R(\omega, T)$. A small fraction of $\mathcal{L}_R(\omega, T)$ is also present in the orthogonal polarization emission, $\mathcal{L}_L(\omega, T) = I_{\mathrm{RL}}(\omega, T) - f(\omega, T) = r(T)\mathcal{L}_R(\omega, T)$, where $r(T) \equiv \frac{I_{\mathrm{RL}}(\omega,T) - f(\omega,T)}{I_{\mathrm{RR}}(\omega,T) - f(\omega,T)}$ is the depolar-

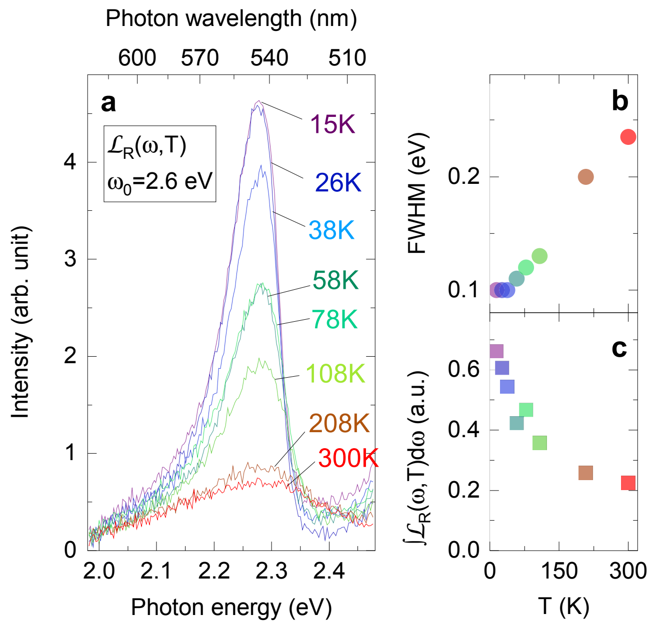

Fig. 4. (a), The intensity of the polarized PL signal, $\mathcal{L}_R(\omega, T)$, as a function of the photon energy for various temperatures. The temperature dependence of, (b), the full-width-at-half-maximum; and (c), the integrated intensity of the polarized PL signal, $\int \mathcal{L}_R(\omega, T)\, d\omega$. The color coding corresponds to the line colors in (a).

ization ratio [see Material and Methods].

In Fig. 4, we plot the temperature dependence of $\mathcal{L}_R(\omega, T)$, excited with 2.6 eV right-circularly polarized light. While PL is much stronger at 15 K, emission remains polarized even at 300 K with same $r(T) \approx 0.1$ for all temperatures [*SI Appendix*, Fig. S6]. This demonstrates that while heating shortens the exciton lifetime, it has little impact on polarization of the exciton emission.

Assuming that the depolarization process occurs mostly during the energy relaxation of the electron and hole within the corresponding bands, we expect $r(T) \to 0$ as ω_0 approaches the direct surface band gap. Figure 1(f) shows that $r(T)$ linearly extrapolates to zero at $\omega_0 \approx 2.5$ eV, which suggests that the band gap should be close to this value. This is consistent with a direct transition between the top branches of RSS and SS2, shown by the blue arrow in Fig. 1(a).

Theoretical model

Surface states. Now we turn to the interpretation of the experimental results. In general, polarization-preserving PL is only possible if the spin degeneracy of electron states is lifted by breaking either time-reversal or inversion symmetries. Since a bulk Bi_2Se_3 crystal is non-magnetic and centrosymmetric, we argue that observed polarized PL must be entirely due to surface bands. In the following, we build a minimal model that explains all the key aspects of the experimental observations, by considering optically excited electrons and holes in SS2 and RSS bands, respectively. Based on the first-principle calculation of the electronic band structure [Fig. 1(b) and *SI Appendix* Fig. S4], we assert that both SS2 and RSS states correspond to $J_z = \pm 1/2$ projections of the total angular momentum on the z-axis and thus can be described by 2×2 Pauli matrices. Also, the mass term in SS2 is by more than a factor of four smaller than the corresponding term in RSS and thus can be neglected [*SI Appendix*, Sec. S2]. With these assumptions, we employ the Hamiltonians

$$\begin{aligned} H_{SS2}(\mathbf{p}) &= \Delta \mathbb{1}_{\sigma_e} + v(\boldsymbol{\sigma}_e \times \mathbf{p}) \cdot \hat{z}, \\ H_{RSS}(\mathbf{p}) &= -\frac{\mathbf{p}^2}{2m_h} \mathbb{1}_{\sigma_h} - \alpha(\boldsymbol{\sigma}_h \times \mathbf{p}) \cdot \hat{z} \end{aligned} \quad [1]$$

to describe the massless Dirac electrons near the SS2 touching point (31) and the massive Rashba holes near the RSS touching point (32), respectively. Here, Δ is the energy difference between the Dirac points of RSS and SS2, v is the Dirac velocity, $m_h > 0$ is the effective hole mass, α is the Rashba coefficient, $\hat{z}$ is a unit vector normal to the surface, $\boldsymbol{\sigma}_e$ and $\boldsymbol{\sigma}_h$ are the vectors of Pauli matrices in the SS2 and RSS spin subspaces, respectively, and $\mathbb{1}_{\sigma_e}$ and $\mathbb{1}_{\sigma_h}$ are the identity matrices in the same subspaces. The linear-in-$\mathbf{p}$ terms describe the effect of SOC which locks electron spin at 90° to its momentum. We note that although the RSS band is not topologically protected, in contrast to the SS1 and SS2 bands, its band parameters are still expected to be universal given atomically smooth and freshly cleaved surfaces, which are realized in Bi_2Se_3.

An interacting electron-hole pair is described by a 4×4 two-body Hamiltonian

$$\begin{aligned} H_{eh}(\mathbf{p}, \mathbf{k}) &= H_{SS2}\left(\mathbf{p} + \tfrac{\mathbf{k}}{2}\right) \otimes \mathbb{1}_{\sigma_h} - \mathbb{1}_{\sigma_e} \otimes H_{RSS}\left(-\mathbf{p} + \tfrac{\mathbf{k}}{2}\right) \\ &\quad + \mathbb{1}_{\sigma_e} \otimes \mathbb{1}_{\sigma_h} V(\mathbf{r}), \end{aligned} \quad [2]$$

where $\mathbf{r} = \mathbf{r_e} - \mathbf{r_h}$ is the relative position of the electron and hole, $V(\mathbf{r})$ describes the Coulomb interaction, $\mathbf{p} = -i\nabla_\mathbf{r}$ and $\mathbf{k}$ is the momentum conjugate to $(1/2)(\mathbf{r_e} + \mathbf{r_h})$. For $\mathbf{k} = 0$, the eigenvalues of $H_{eh}(\mathbf{p}, \mathbf{k})$ have a W-shaped dispersion resembling a multi-layer Mexican hat [cf. Figs. 1(d) and S2 in *SI Appendix*]. If both electron and hole bands were massless, a bound state would not be possible. However, the two-body bands originating from $H_{eh}(\mathbf{p}, 0)$ are bounded from below for any values of v and α by the $\mathbf{p}^2$ term in the RSS band. Therefore, the Coulomb attraction between electrons and holes lead to excitonic bound states.

Eigenstates and optical transitions. In what follows, we focus on the case of zero total momentum ($\mathbf{k} = 0$) appropriate for direct optical transitions studied in this Report. If $V(\mathbf{r})$ is axially symmetric, the z component of the angular momentum of an electron-hole pair

$$\hat{J}_z = \mathbb{1}_{\sigma_e} \otimes \mathbb{1}_{\sigma_h}(-i\partial_\phi) + \frac{1}{2}\mathbb{1}_{\sigma_e} \otimes \sigma_h^z + \frac{1}{2}\sigma_e^z \otimes \mathbb{1}_{\sigma_h} \quad [3]$$

is a good quantum number although neither the orbital angular momentum nor spin are good quantum numbers on their own. (Here, ϕ is the azimuthal angle of $\mathbf{p}$.) Therefore, the eigenstates of Eq. (2) can be classified by J_z. The Schrödinger equation defined by the Hamiltonian in Eq. (2) can be solved by the following Ansatz for the 4-component spinor wavefunction in the momentum-space representation [*SI Appendix*, Sec. S1B]:

$$\psi(\mathbf{p}) = e^{iJ_z\phi}\left(\psi_1(p)e^{-i\phi}, \psi_2(p), \psi_3(p), \psi_4(p)e^{i\phi}\right)^T, \quad [4]$$

where $p \equiv |\mathbf{p}|$. To understand the general properties of the resulting discrete states and, in particular, their spin structure, it is instructive to replace the interaction potential by a model short-range attraction $V(\mathbf{r}) = -\lambda\delta(\mathbf{r})$, which provides a reasonable approximation for Coulomb interaction screened by free carriers. In this case, algebraic equations for amplitudes $\psi_1(p),\dots,\psi_4(p)$ have non-trivial solutions for an infinitesimally small λ, but only for states with $J_z=0$ and $J_z=\pm1$ [*SI Appendix, Sec. S1A*]. The bound states with $J_z=\pm1$, labeled as $|J_z=\pm1\rangle$ in Fig. 1(d), are doubly degenerate, whereas the two states with $J_z=0$, labeled as $|J_z=0\rangle$, have different energies[†]. Within the backscattering geometry of our experiment, circularly polarized light can only produce excitations with $\Delta J_z=\pm1$. Assuming no cross-relaxation between $|J_z=\pm1\rangle$ and $|J_z=0\rangle$ states, we expect a single PL peak arising from recombination of the $|J_z=\pm1\rangle$ exciton, which is consistent with the data [Fig. 1(c)].

The above argument is suitable for explaining polarized PL excited by photons with energies close to the Mexican-hat minimum of Fig. 1(d). One could expect that scattering by phonons couples the $|J_z=+1\rangle$ and $|J_z=-1\rangle$ states for energies above the minimum, which would cause an increase of $r(T)$ with ω_0. However, we see only a moderate increase of $r(T)$ even if ω_0 is about 300 meV above the Mexican-hat minimum [Fig. 3]. To explain the preservation of optical orientation during energy relaxation, we note that a transition between the $|J_z=\pm1\rangle$ states requires non-fully symmetric scattering channels that does not commute with $\hat{J}_z$. However, it is known that non-symmetric surface phonons in Bi_2Se_3 are weak (34, 35), leaving J_z approximately conserved during the energy relaxation. It would be interesting to study in the future the interaction between the chiral exciton and other more exotic collective modes, such as the Dirac plasmons and chiral spin modes (27, 36, 37). Importantly, the $|J_z=\pm1\rangle$ exciton states can also be resonantly populated with circularly polarized 2.3 eV excitation [Fig. 3], which suggests that the exciton states are dipole-allowed and thus confirms the proposed model.

Bound state energies. The theoretical model described above allows one to extract quantitative characteristics of the exciton spectra. The exciton energies for a short-range interaction as functions of the dimensionless coupling constant $u=m_h\lambda/2\pi\hbar^2$ are shown in Fig. 5. With the band parameters extracted from ARPES data (17, 18), one finds for the absorption edge in the $J_z=\pm1$ channel $E_g^{\pm1}=\Delta-m_h(\alpha+v)^2/2\approx1.8$ eV, which is somewhat smaller but comparable to the observed value of 2.48 eV. For a more realistic case of the Coulomb interaction (which is assumed to be weak), the binding energy can be estimated as $\epsilon_{\pm1}-E_g^{\pm1}=-4\mathrm{Ry}^*\ln^2\left[2m_h(\alpha+v)a_B/\mathrm{e}^2\hbar\right]$ (38, 39), where $\mathrm{Ry}^*=m_he^4/2\hbar^2\varepsilon_{\mathrm{eff}}^2\approx0.02$ eV is the effective Rydberg, $\varepsilon_{\mathrm{eff}}\approx13$ is the effective dielectric constant of semi-infinite Bi_2Se_3 for frequencies above the topmost phonon mode, $a_B=\hbar^2\varepsilon_{\mathrm{eff}}/m_he^2$ is the effective Bohr radius, and $\mathrm{e}=2.718\dots$ is the base of the natural logarithm. The (large) logarithmic factor in the bound state energy arises because massive holes with energies close to the minimum of the Rashba spectrum exhibit an effectively one-dimensional (1D) motion (38). In 1D, the bound state energy in a weak potential $U(x)$ is proportional to $\left[\int dxU(x)\right]^2$ (40), hence the $\ln^2$ factor for the $1/x$ potential. A more accurate result can be obtained

[†] Strictly speaking, exciton states have to be classified within the surface symmetry group, which is C_{6v} for actual Bi_2Se_3 (33) or $C_{\infty v}$ for a rotationally-invariant Hamiltonian in Eq. (2). Inspecting the exciton wave functions in Eq. (4), we find that the two $|J_z=0\rangle$ states are fully symmetric with respect to all symmetry operators of both C_{6v} and $C_{\infty v}$ groups, and therefore belong to the A_1 irreducible representation. On the other hand, the doubly degenerate $|J_z=\pm1\rangle$ states belong to the E_1 representation, which transform as an in-plane electric dipole.

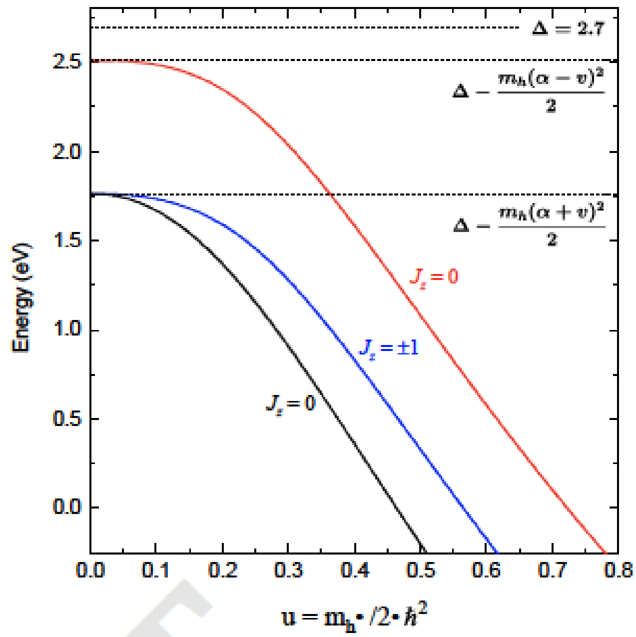

Fig. 5. Bound state energies of excitons with $J_z=\pm1$ (blue) and $J_z=0$ (red and black) obtained by numerically diagonalizing Eq. (2) with $V(\mathbf{r})=-\lambda\delta(\mathbf{r})$. The band structure parameters are taken from fitting the ARPES data of Refs. (17) and (18) into the spectrum of Eq. (1): $\Delta=2.7$ eV, $v=2.0$ eVÅ, $\alpha=5.2$ eVÅ, $m_h=0.036\,\mathrm{eV}^{-1}\mathrm{Å}^{-2}$ [*SI Appendix*, Sec. S2], and $u=m_h\lambda/2\pi\hbar^2$.

by numerical solution of the Schrödinger equation (39) which gives 0.22 eV for the bound state energy, whereas the observed value is 0.2 eV. We thus conclude that our theoretical model is in quantitative agreement with the data.

We note that while α and v may vary slightly from sample to sample, the chiral exciton energy depends only logarithmically on the band structure parameters, at least as long as the Coulomb attraction between electron and hole is sufficiently weak. Furthermore, it is known from ARPES measurements, nonlinear optics, and first principle calculations that, while the the position of the Fermi level is very sensitive to surface preparation, the surface states are rather robust against (nonmagnetic) surface dopants (21, 41, 42). In our case, the surface states composing the chiral exciton are far away from the Fermi level, and thus should be even less sensitive to surface contamination. This naturally explains the reproducibility of the observed features between samples.

Conclusions

We used polarization-resolved photoluminescence (PL) spectroscopy to study the secondary emission from the surface states of an archetypical topological insulator Bi_2Se_3. When the crystal is excited with 2.5–2.8 eV circularly polarized light, we detect emission of the same polarization at 2.3 eV. Polarization of emitted light is preserved even if the excitation energy is hundreds of meVs above the emission threshold energy. We assign such emission as resulting from recombination of novel exciton states: *chiral excitons.* We propose that chiral excitons are made of (topologically protected) massless electrons and massive holes, both residing on the surface of Bi_2Se_3 and characterized by chiral spin textures. The exciton states can be characterized by the eigenvalues of the out-of-plane total angular momentum, J_z. Based on the results of our theoretical model, we identify the doublet of degenerate states with $J_z = \pm 1$ as being responsible for observed polarization-preserving PL. The most surprising finding is that polarization of chiral exciton PL is preserved up to room temperature and robust with respect to chemical substitution, which we attribute to the weakness of spin-flip scattering between surface states with opposite helicity. In this way, chiral excitons are fundamentally different from other known excitons that also preserve helicity (4, 13). Controlled optical orientation of chiral surface excitons may facilitate new photonics and optoelectronics applications of topological insulators.

Materials and Methods

Material growth. All data presented in the main text are collected from bulk single crystals grown by modified Bridgman method. Mixtures of high-purity bismuth (99.999%) and selenium (99.999%) with the mole ratio Bi : Se = 2 : 3 were heated up to 870 °C in sealed vacuum quartz tubes for 10 hours, and then slowly cooled to 200 °C with rate 3 °C/h, followed by furnace cooling to room temperature.

Experimental setup. The crystals were cleaved prior to cool down in a glove bag filled with nitrogen gas, and were transferred into a continuous flow liquid helium optical cryostat without exposure to atmosphere. A solid state laser was used for 2.33 eV (532 nm) excitation, a diode laser was used for 2.77 eV (447 nm) excitation, and a Kr^{+} ion laser was used for all other excitations, with laser spot size roughly $50 \times 50\,\mu m^2$. The power density on the sample is kept below $0.7\,\mathrm{kW/cm^2}$, and all temperatures shown were corrected for laser heating with 1 K/mW. The polarized secondary emission was analyzed and collected by a custom triple-grating spectrometer with a liquid nitrogen cooled CCD detector.

The intensity $I_{\mu\nu}(\omega, T)$, was corrected for the laser power and spectral response of the spectrometer and CCD, where μ (ν) denotes the direction of incident (collected) photon polarization, ω is energy and T is temperature. The scattering geometries used in this experiment are denoted as $\mu\nu$ =RR, RL, XX and YX. $\mathrm{R} = \mathrm{X} + i\mathrm{Y}$ and $\mathrm{L} = \mathrm{X} - i\mathrm{Y}$ denotes the right- and left-circular polarizations, respectively, where X (Y) denotes linear polarization parallel (orthogonal) to the plane of incidence. Here, we follow the "spectroscopy convention" for the "handedness" of circularly polarized light. That is, the right and left polarization refers to the angular momentum measured in the lab frame, rather than the helicity of photon.

Photoluminescence background subtraction. With right circularly polarized excitation, the measured PL intensities can be decomposed into two parts:

$$\begin{aligned} I_{\mathrm{RR}}(\omega,T) &= \mathcal{L}_R(\omega,T) + f(\omega,T) \\ I_{\mathrm{RL}}(\omega,T) &= \mathcal{L}_L(\omega,T) + f(\omega,T) \end{aligned} \qquad [5]$$

Where $\mathcal{L}_R(\omega,T)$ and $\mathcal{L}_L(\omega,T)$ denotes right and left circularly polarized PL, respectively, and $f(\omega,T)$ denotes the featureless unpolarized broad background. We assume an energy independent depolarization ratio $r(T) = \frac{\mathcal{L}_L(\omega,T)}{\mathcal{L}_R(\omega,T)}$. Inserting $r(T)$ into the above expression of $I_{\mathrm{RL}}(\omega,T)$, we can write the unpolarized emission as:

$$f(\omega,T) = \frac{I_{\mathrm{RL}}(\omega,T) - r(T)\cdot I_{\mathrm{RR}}(\omega,T)}{1-r(T)}. \qquad [6]$$

Then, $r(T)$ is determined by minimizing sharp features in $f(\omega,T)$ around the 2.3 eV PL peak. The circularly polarized PL can be calculated knowing $r(T)$,

$$\mathcal{L}_R(\omega,T) = \frac{I_{\mathrm{RR}}(\omega,T) - I_{\mathrm{RL}}(\omega,T)}{1-r(T)}. \qquad [7]$$

ACKNOWLEDGMENTS. We are grateful for technical support from B.S. Dennis and A. Rustagi, and discussions with L.S. Levitov, Z. Lu, E.I. Rashba, Z.X. Shen, D. Smirnov, J.A. Sobota, H. Soifer and D. Vanderbilt. We acknowledge support from NSF DMR-1104884 (G.B., H.-H.K and A.L.), NSF DMR-1720816 (D.L.M.), and NSF DMREF Grant DMR-1629059 (S.-W.C. and X.W.).

1. Žutić I, Fabian J, Das Sarma S (2004) Spintronics: Fundamentals and applications. *Rev. Mod. Phys.* 76(2):323.
2. Shekhter A, Khodas M, Finkel'stein AM (2005) Chiral spin resonance and spin-Hall conductivity in the presence of the electron-electron interactions. *Phys. Rev. B* 71(16):165329.
3. Mak KF, Shan J (2016) Photonics and optoelectronics of 2D semiconductor transition metal dichalcogenides. *Nat. Photon.* 10(4):216–226.
4. Planel R, Guillaume C (1984) *Optical Orientation of Excitons.* (Elsevier Science Ltd), p. 353.
5. D'Yakonov MI (2017) *Spin Physics in Semiconductors.* (Springer International Publishing).
6. Parsons RR (1969) Band-To-Band Optical Pumping in Solids and Polarized Photoluminescence. *Phys. Rev. Lett.* 23(20):1152–1154.
7. Ekimov AI, Safarov VI (1970) Optical orientation of carriers in interband transitions in semiconductors. *Soviet Journal of Experimental and Theoretical Physics Letters* 12:198.
8. Zakharchenya BI, Fleisher VG, Dzhioev RI, Veshchunov YP, Rusanov IB (1971) Effect of optical orientation of electron spins in a GaAs crystal. *Soviet Journal of Experimental and Theoretical Physics Letters* 13:137.
9. Gross E, Permogorov S, Morozenko Y, Kharlamov B (1973) Hot-exciton luminescence in CdSe crystals. *physica status solidi (b)* 59(2):551–560.
10. Bonnot A, Planel R, à la Guillaume CB (1974) Optical orientation of excitons in CdS. *Phys. Rev. B* 9(2):690–702.
11. Subashiev A, Mamaev Y, Oskotskii B, Yashin Y, Kalevich V (1999) Effects of heavy p doping on the polarized emission spectra and low-temperature luminescence spectra of GaAs/GaAsP strained-layer structures. *Semiconductors* 33(11):1182–1187.
12. Mak KF, He K, Shan J, Heinz TF (2012) Control of valley polarization in monolayer MoS_2 by optical helicity. *Nat. Nanotechnol.* 7(8):494–498.
13. Xu X, Yao W, Xiao D, Heinz TF (2014) Spin and pseudospins in layered transition metal dichalcogenides. *Nature Phys.* 10(5):343–350.
14. Jones AM, et al. (2013) Optical generation of excitonic valley coherence in monolayer WSe_2. *Nat. Nanotechnol.* 8(9):634–638.
15. Qiu DY, da Jornada FH, Louie SG (2013) Optical Spectrum of MoS_2: Many-Body Effects and Diversity of Exciton States. *Phys. Rev. Lett.* 111(21):216805.
16. Gmitra M, Fabian J (2015) Graphene on transition-metal dichalcogenides: A platform for proximity spin-orbit physics and optospintronics. *Phys. Rev. B* 92(15):155403.
17. Sobota JA, et al. (2013) Direct Optical Coupling to an Unoccupied Dirac Surface State in the Topological Insulator Bi_2Se_3. *Phys. Rev. Lett.* 111(13):136802.
18. Soifer H, et al. (2017) Band resolved imaging of photocurrent in a topological insulator.
19. Hsieh D, et al. (2009) A tunable topological insulator in the spin helical Dirac transport regime. *Nature* 460(7259):1101–1105.
20. Zhang H, et al. (2009) Topological insulators in Bi_2Se_3, Bi_2Te_3 and Sb_2Te_3 with a single Dirac cone on the surface. *Nature Phys.* 5(6):438.
21. Chen YL, et al. (2009) Experimental realization of a three-dimensional topological insulator, Bi_2Te_3. *Science* 325(5937):178–181.
22. Qi XL, Zhang SC (2011) Topological insulators and superconductors. *Rev. Mod. Phys.* 83(4):1057–1110.
23. Hasan MZ, Moore JE (2011) Three-dimensional topological insulators. *Annual Review of Condensed Matter Physics* 2(1):55–78.
24. Bugini D, et al. (2017) Ultrafast spin-polarized electron dynamics in the unoccupied topological surface state of Bi_2Se_3. *Journal of Physics: Condensed Matter* 29(30):30LT01.
25. Valdés Aguilar R, et al. (2012) Terahertz Response and Colossal Kerr Rotation from the Surface States of the Topological Insulator Bi_2Se_3. *Phys. Rev. Lett.* 108(8):087403.
26. Wu L, et al. (2016) Quantized Faraday and Kerr rotation and axion electrodynamics of a 3D topological insulator. *Science* 354(6316):1124.
27. Kung HH, et al. (2017) Chiral Spin Mode on the Surface of a Topological Insulator. *Phys. Rev. Lett.* 119(13):136802.
28. Shao Y, et al. (2017) Faraday rotation due to surface states in the topological insulator $(Bi_{1-x}Sb_x)_2Te_3$. *Nano Letters* 17(2):980–984.
29. Liu Q, et al. (2015) Search and design of nonmagnetic centrosymmetric layered crystals with large local spin polarization. *Phys. Rev. B* 91(23):235204.
30. Vinattieri A, et al. (1994) Exciton dynamics in GaAs quantum wells under resonant excitation. *Phys. Rev. B* 50(15):10868–10879.
31. Fu L (2009) Hexagonal Warping Effects in the Surface States of the Topological Insulator Bi_2Te_3. *Phys. Rev. Lett.* 103(26):266801.
32. Winkler R (2003) *Spin–Orbit Coupling Effects in Two-Dimensional Electron and Hole Systems.* (Springer Berlin / Heidelberg).
33. Li J, Tu JJ, Birman JL (2013) Symmetry predicted transitions in 3D topological insulators. *Solid State Communications* 163:11 – 14.
34. Kung HH, et al. (2017) Surface vibrational modes of the topological insulator Bi_2Se_3 observed by Raman spectroscopy. *Phys. Rev. B* 95(24):245406.
35. Sobota JA, et al. (2014) Distinguishing Bulk and Surface Electron-Phonon Coupling in the Topological Insulator Bi_2Se_3 Using Time-Resolved Photoemission Spectroscopy. *Phys. Rev. Lett.* 113(15):157401.
36. Raghu S, Chung SB, Qi XL, Zhang SC (2010) Collective Modes of a Helical Liquid. *Phys. Rev. Lett.* 104(11):116401.
37. Politano A, et al. (2015) Interplay of Surface and Dirac Plasmons in Topological Insulators: The Case of Bi_2Se_3. *Phys. Rev. Lett.* 115(21):216802.
38. Chaplik AV, Magarill LI (2006) Bound States in a Two-Dimensional Short Range Potential Induced by the Spin-Orbit Interaction. *Phys. Rev. Lett.* 96(12):126402.
39. Grimaldi C (2008) Energy levels of a two-dimensional hydrogen atom with spin-orbit rashba interaction. *Phys. Rev. B* 77(11):113308.
40. L. D. Landau and E. M. Lifshitz (1977) *Quantum Mechanics (Non-relativistic Theory).* (Perg-

amon Press, New York).
41. Hsieh D, et al. (2011) Nonlinear Optical Probe of Tunable Surface Electrons on a Topological Insulator. *Phys. Rev. Lett.* 106(5):057401.
42. Koleini M, Frauenheim T, Yan B (2013) Gas doping on the topological insulator Bi_2Se_3 surface. *Phys. Rev. Lett.* 110(1):016403.